International Journal of Greenhouse Gas Control 20 (2014) 168–179

Contents lists available at ScienceDirect

International Journal of Greenhouse Gas Control

journal homepage: www.elsevier.com/locate/ijggc

Numerical assessment of CO_2 geological sequestration in sloping and layered heterogeneous formations: A case study from Taiwan

Rui-Tang Sung[a], Min-Hsu Li[a,*], Jia-Jyun Dong[b], Andrew Tien-Shun Lin[c], Shu-Kun Hsu[c], Chien-Ying Wang[c], Chien-Nan Yang[c]

[a] Graduate Institute of Hydrological and Oceanic Sciences, National Central University, No. 300, Jhongda Road, Jhongli, Taiwan
[b] Graduate Institute of Applied Geology, National Central University, No. 300, Jhongda Road, Jhongli, Taiwan
[c] Department of Earth Sciences, National Central University, No. 300, Jhongda Road, Jhongli, Taiwan

ARTICLE INFO

Article history:
Received 23 May 2013
Received in revised form
26 September 2013
Accepted 7 November 2013

Keywords:
CO_2 geological sequestration
Changhu Coastal Industrial Park (CCIP) site
Taiwan
TOUGHREACT/ECO2N

ABSTRACT

Carbon dioxide geological sequestration (CGS) has been recognized as one of the potential solutions for reducing anthropogenic CO_2 emissions. The Changhua Coastal Industrial Park (CCIP) in central Taiwan has been preliminarily evaluated as a potential site for CGS. The CCIP site possesses sloping and layered heterogeneous formations with stagnant groundwater flow. Previous geophysical investigations of seismic reflection survey have found no significant faults near this site. Prior to the actual application of CGS in the field, it is important to carry out numerical simulations to predict the short- and long-term evolution of injected CO_2 into deep geological formations. In this study, the TOUGHREACT/ECO2N simulator is employed in order to conduct comprehensive CGS assessments at the CCIP site. Field scale CGS simulations are utilized to capture the details of the physical features, such as the displacement of saline brine by the injection of CO_2, buoyancy/gravity convection, and salt precipitation due to pore water dry-out, in the vicinity of the CO_2 injection well. Simulation results show that (1) the migration of CO_2 plume did not penetrate the low permeability formation at 500 years, (2) formation tilting caused a slightly asymmetric CO_2 plume oriented toward the up-tilt direction, and (3) the amount of solubility and residual gas trapping accounted for 26.8% and 19.0%, respectively, of injected CO_2 by weight at 500 years.

1. Introduction

Coal-fired power plants contribute about 40% of the total annual power generation in Taiwan. About 81.4 million tons of CO_2 emissions per year are produced by thermal power generation, with more than 70% of those emissions generated by coal-fired power plants (Taiwan Power Company, 2008–2013). Awareness of global warming has made the reduction of CO_2 emissions produced by the energy sector inevitable and a necessary part of the national policy in Taiwan (Taiwan Power Company, 2009; Chiao et al., 2010). Among several greenhouse gas control measures, CO_2 geological sequestration (CGS), which is accomplished by injecting CO_2 captured from fossil fuel power plants into deep saline brine geological formations, has been recognized as one way to reduce anthropogenic CO_2 emissions (e.g., Bachu et al., 1994; Pruess and García, 2002; Doughty et al., 2004; Juanes et al., 2006; Class et al., 2009; Xu et al., 2011; Yu et al., 2011; Zhang et al., 2011).

Extensive thick sedimentary rock formations have been found on the west side of the Central Mountain Range facing the Taiwan Strait (Lin and Watts, 2002). These formations contain a well-developed sedimentary environment comprised of multiple layers of reservoirs and lower permeability layers which have the potential to provide a massive volume for CGS storage (Fig. 1). However, owing to its location on the convergent boundary between the Eurasian plate and the Philippine Sea plate, Taiwan is one of the most seismically active regions in the world (Wang and Shin, 1998). Many studies have shown that the existence of faults and earthquake activity may limit sequestration capacity and could damage the integrity of the sealing barrier (e.g., Pruess and García, 2002; Celia and Nordbotten, 2009; Todaka et al., 2009). Previous investigations have identified three potential formations suitable for CGS in the Taiwan area, the Kuanyin Plateau (in Northern Taiwan), the Taishi Basin (in Central Taiwan), and the Tainan Basin (in Southern Taiwan) (see Fig. 1), where faults are few and there is a low density of epicenters (Bonilla, 1975; Lin et al., 2000; Lin and Watts, 2002; Cheng et al., 2007).

The major sources of CO_2 emissions in Taiwan are thermal power plants (primarily coal-fired), refineries, petrochemical plants, steel plants, and cement plants. The annual amount of CO_2

* Corresponding author. Tel.: +886 34227151x65691.
E-mail address: mli@cc.ncu.edu.tw (M.-H. Li).

1750-5836/$ – see front matter © 2013 Elsevier Ltd. All rights reserved.
http://dx.doi.org/10.1016/j.ijggc.2013.11.003

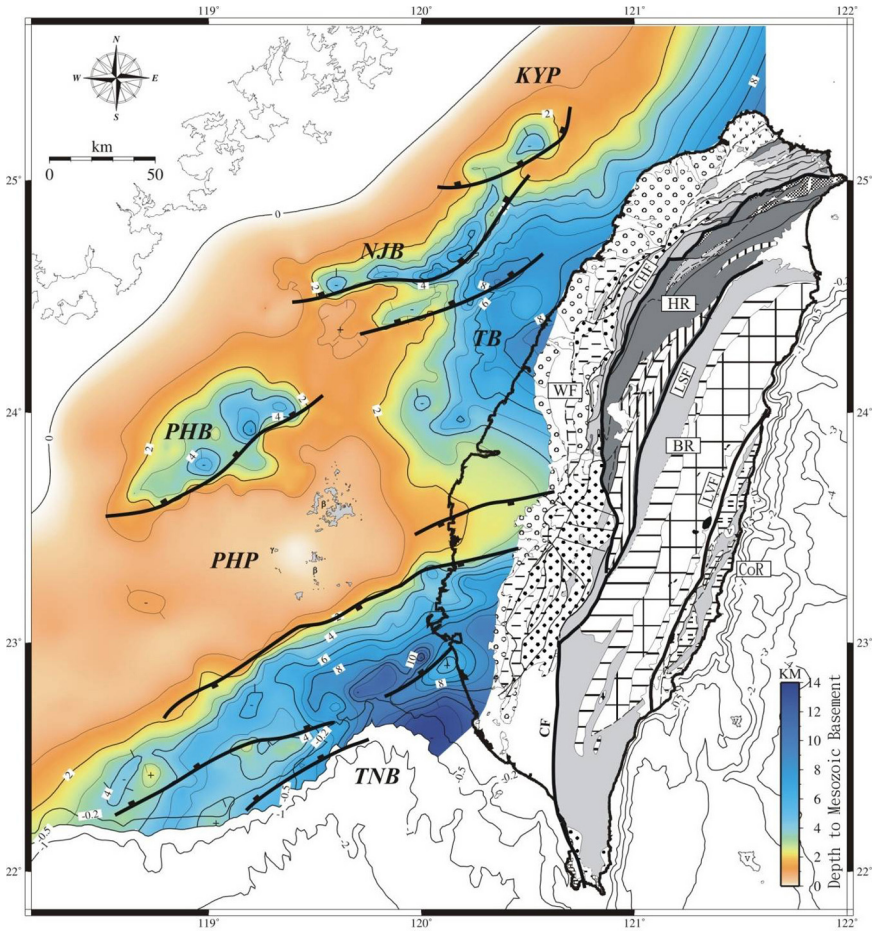

Fig. 1. Map of the sedimentary formations along the Taiwan Strait (modified from Lin et al. (2003)). KYP, TB, and TNB represent the Kuanyin Plateau, Taihsi Basin, and Tainan Basin, respectively.

emissions is about 200 Mt/yr with major sources located along the western coastline. By 2025, about 90 Mt/yr needs to be geo-sequestered in order to meet the government's green initiatives. The Changhua Coastal Industrial Park (CCIP) site, located in the southern Taihsi Basin is viewed as a good potential CGS site because of its proximity to massive stationary sources of CO_2 emissions from nearby petrochemical and coal-fired power plants (Chiao et al., 2010; Yu et al., 2011). In the vicinity is a major emitter, the Taichung Power Plant (36.3 Mt/yr), which is actually the largest coal-fired power plant in the world. (Taiwan Power Company, 2010). About 50 km south of the CCIP site, the large stationary emitters include the Mailiao Petrochemical Plant (2.7 Mt/yr) and the Mailiao Power Plant (25.3 Mt/yr).

Sloping and layered heterogeneous sedimentary formations are commonly observed along the coastal plate of western Taiwan. Analytical and semi-analytical evaluations have been performed in past studies to assess CGS practices on the basin scale (e.g., Nordbotten and Celia, 2006; Hesse et al., 2008; Nicot, 2008; MacMinn et al., 2010, 2011; Gasda et al., 2011). Only a few studies have focused on numerical assessments for sloping and layered heterogeneous sedimentary formations on the field scale (e.g., Doughty et al., 2004; Yamamoto et al., 2009; Elenius et al., 2010; Pruess and Nordbotten, 2011). In this study, locally refined grids were generated to facilitate simulation with the TOUGHRE-ACT/ECO2N simulator of the aquifer responses and the behavior of the migration of CO_2 plume during and following CO_2 injection.

The objectives of this study include the following: (1) to understand the aquifer responses and the behaviors of CO_2 plume migration during and following CO_2 injection into sloping and layered heterogeneous sedimentary formations; (2) to assess the safety of CO_2 plume leakage; and (3) to identify the dominant CO_2 trapping mechanisms (hydrodynamic trapping, residual gas trapping, and solubility trapping) at the study site.

2. Geophysical investigation and site description

2.1. Geophysical investigation: seismic reflection survey

The Taihsi Basin is located along the coastal area in Northern and Central Taiwan, from Shinchu County to Changhua County, as shown in Fig. 1. Previous geological investigation has suggested that the Taihsi Basin is comprised of formations from the latest Miocene age to the recent age and comprises a coarsening upward sequence of shallow water clastics and fluvial sediments (Lin and Watts, 2002). The block outlined with red solid lines in Fig. 1 shows, the region of the southern Taihsi Basin, covering the area from the Taichuang Port to the mouth of the Chuoshui River. This is identified as one of the most favorable potential sites for CGS due to the relative lack of unfavorable geological structures (e.g., faulted and folded structures) and low seismic activity (Chiao et al., 2010; Yu et al., 2011). Another advantage in the south Taihsi Basin is the thickness of the sedimentary formations which become thinner toward the southwest, as shown in Fig. 1. The detailed geophysical investigations conducted in the south Taihsi Basin include both onshore and offshore seismic reflection surveys aimed at understanding the geological structures of the south Taihsi Basin in association with a previous deep borehole investigation at the

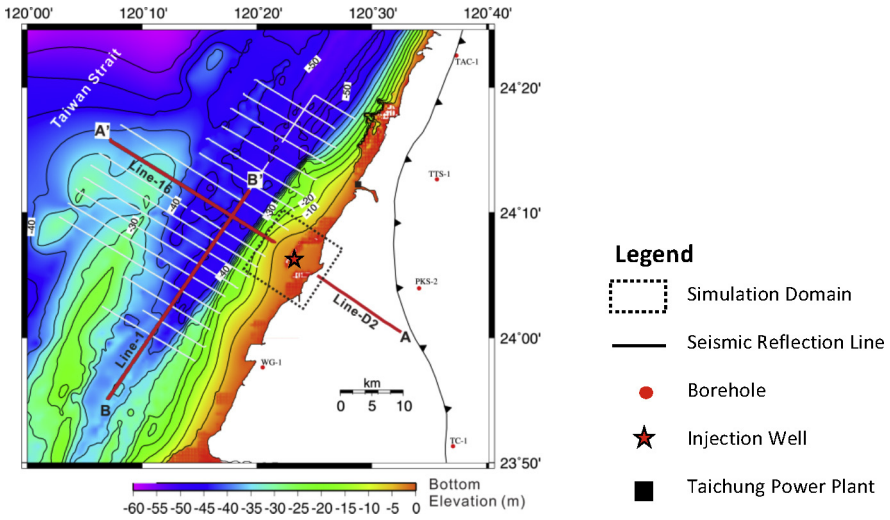

Fig. 2. Map of the study area – Changhua Coastal Industrial Park Site and survey lines of seismic reflection. The shading indicates the bottom elevation of Taiwan Strait.

WG-1 well, as shown in Fig. 2, which corresponds to the block outlined with red solid lines depicted in Fig. 1.

Fig. 3 shows the A–A′ and B–B′ geological profiles (indicated in Fig. 2) revealed from seismic reflection surveys, interpreted in association with WG-1 borehole logs. The geological cross-section of A–A′ obtained by merging offshore survey line (OR1-928-16) and onshore survey line (D2) is shown in Fig. 3a. It should be noted that seismic surveys encounter difficulties when the water

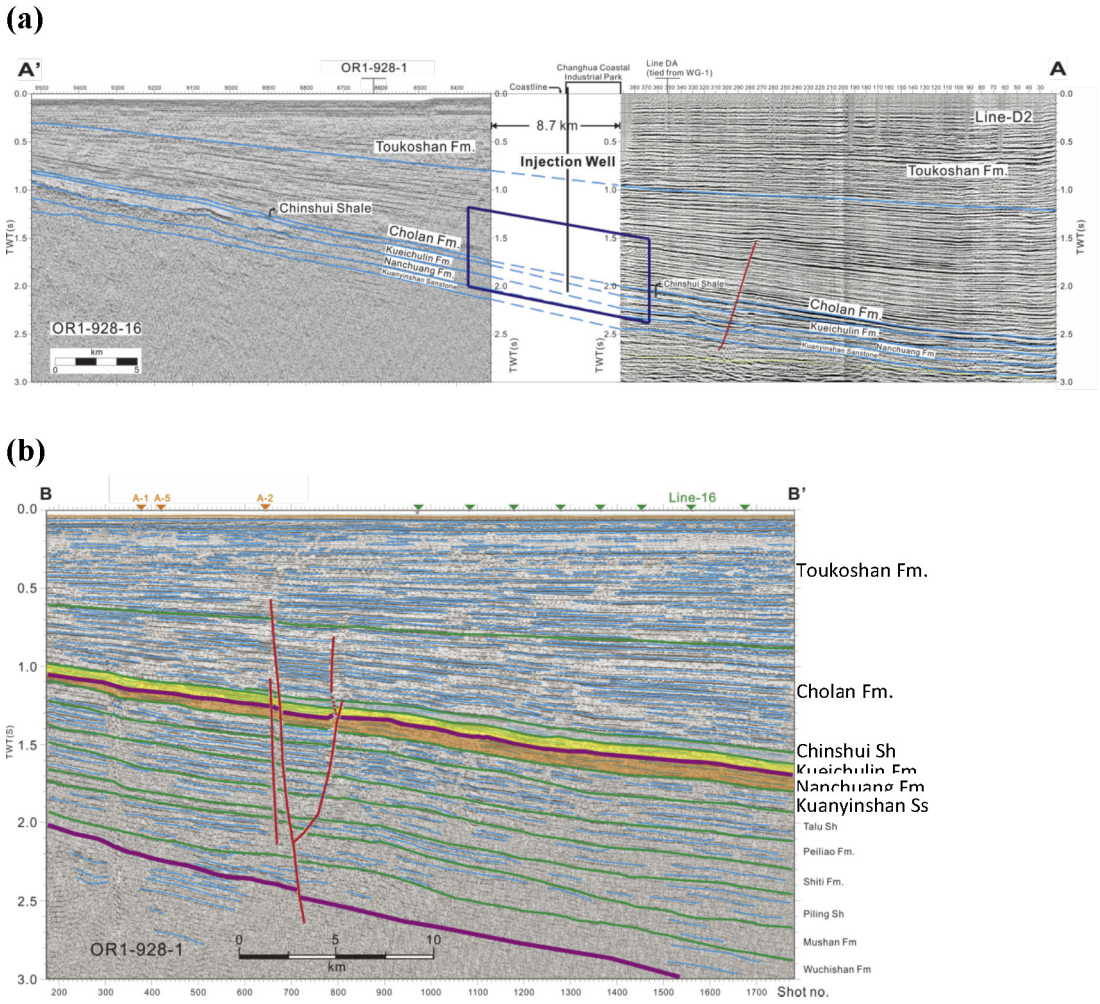

Fig. 3. (a) A–A′ geological cross-section (across the shoreline) interpreted from two survey lines of OR1-928-16 (in offshore area) and D2 (in onshore area) and (b) B–B′ geological cross-section (along the shoreline) interpreted from a survey line of OR1-928-1. Locations of selected survey lines are shown in Fig. 2. The term of TWT (abbreviation for the two way time) shown on the left of both figures is the time taken for a surface-generated seismic wave to reach a subsurface rock layer and return to the surface.

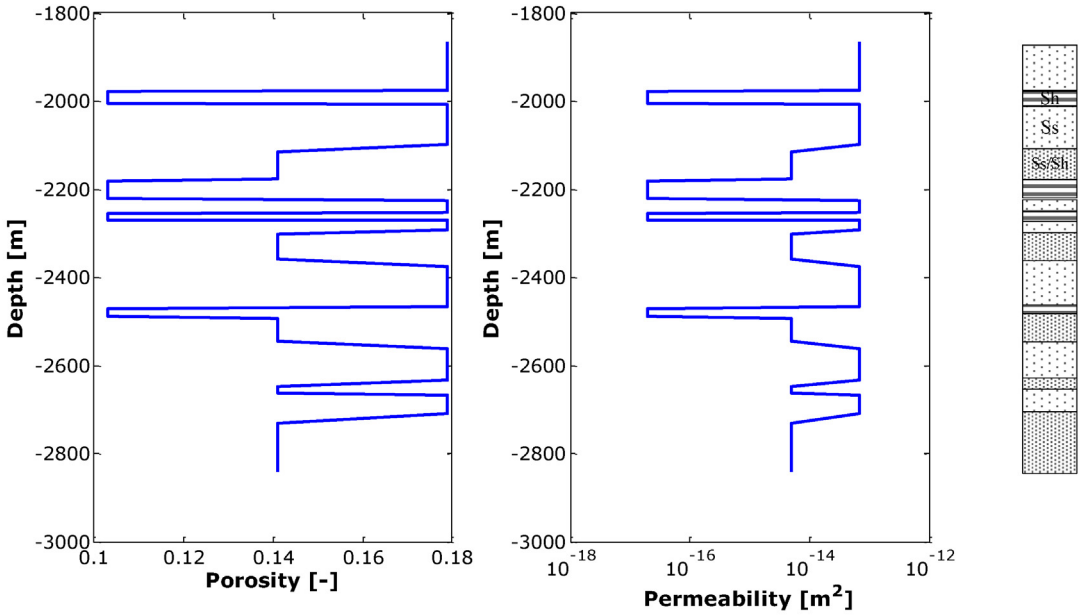

Fig. 4. Rock properties profiles for the CO_2 injection well at the CCIP site: porosity (left panel), permeability (middle panel) and rock type (right panel). Ss, Sh, and Ss/Sh represent the sandstone, shale, and interbedded sandstone and shale, respectively.

is too shallow or subject to changes in depth, especially within the tidal zones. Therefore, due to such technical difficulties, a blank area exists between OR1-928-16 and D2. Linear interpolationis used to link geological formations retrieved from two survey lines. The geological cross-section B–B′ is interpreted from the seismic reflection survey line of OR1-928-1 as shown in Fig. 3b. A developing fault exists across the formations between the lower part of Toukoshan Fm. (Formation) and Talu Shale shown in cross-section A–A′. Fork shaped faults also existed across the formations between the lower part of the Toukoshan Fm. and the deeper formations in cross-section B–B′. Due to seaward sloping formations and the location of potential sites, the onshore fault identified by the line A–A′ in the seismic reflection survey is located downstream of the injection well, and thus there is less possibility of leakage through the fault during the migration of CO_2 that may be injected in the future. On the other hand, the offshore fault, identified by line B–B′ in the seismic reflection survey, is located on the up-tilt side far away from the potential CGS reservoir at the CCIP. At the current stage, both faults will not be considered in our simulations.

2.2. Site description

The Changhua Coastal Industrial Park (CCIP; 120.38°E, 24.11°N) is a land reclamation projects in Central Taiwan (Fig. 2) that has been preliminarily evaluated as a potential site for CGS practices. The geological formation in CCIP Site is a part of the Southern Flank of the Taihsi Basin. The geological characteristics of the CCIP site show sloping and layered heterogeneous formations with stagnant groundwater flow. As described in the previous section, the sequential sedimentary formations from the ground surface to deep deposition include the Toukoshan Fm., Cholan Fm., Chinshui Shale, Kueichulin Fm., Nanchuang Fm., and Kuanyinshan Sandstone as noted in Fig. 3b. With the exception of the Toukoshan Fm., most formations contain interbedded materials comprised of sandstone, siltstone, and shale (Dong et al., 2010; Chiao et al., 2010). The sedimentary formations gradually becomes thinner toward the seaward direction. Although the CCIP site is located on the deformation front west of Taiwan which has developed due to the convergent boundary between the Eurasian plate and the Philippine Sea plate, previous seismic investigations have found no significant faults and few records of associated earthquake events in this area (Bonilla, 1975; Lin et al., 2000; Lin and Watts, 2002; Cheng et al., 2007). There are only two major faults observed but these are far downstream of the CCIP site (as described in the previous section). According to seismic reflection surveys and WG-1 borehole logs, the region between the lower part of the Cholan Fm. and upper part of the Kuanyinshan Sandstone can be identified as a suitable reservoir for CGS. The domain of interest (side view) in association with survey lines and the location of the injection well that is simulated in this study are shown with dark blue solid lines and a black vertical line, respectively, in Fig. 3a. The top view of the simulation domain is shown in the block outlined with black dashed lines in Fig. 2.

3. Simulation setup

3.1. Hydrogeology settings

The conceptual 3-D lithological model for our simulation domain is constructed using data from two seismic scanning reflection survey lines (along shore B–B′ and cross shore A–A′) and one well drilled for geological investigation (WG-1) near the CCIP site, as shown in Fig. 2. Fig. 4 shows profiles of the properties of the rock in the CO_2 injection well which have been estimated from the borehole lithology data. The profiles, from the lower part of the Cholan Fm. to the upper part of the Kuanyinshan Sandstone, are obtained with a linear interpolation method. A relatively low permeable layer of Chinshui Shale is identified approximately 2469–2490 m below the mean sea level which acts as the low permeability caprock in the CGS simulations (see Fig. 4). The potential CGS reservoir consists of sandstone and interbedded of sandstone/siltstone and shale that lies beneath the Chinshui Shale (Chiao et al., 2010; Yu et al., 2011). Due to computational limitations, the detailed layers of sedimentary formations realized from borehole logs needed to be simplified. Three types of rock, sandstone (Ss), shale (Sh), and interbedded sandstone and shale (Ss/Sh), are considered in the conceptualized lithology model.

Table 1
Estimated hydrogeological parameters for the CCIP site.

Rocks	Permeability[a] [m^2]	Porosity [−]
Sandstone (Ss)	6.70×10^{-14}	0.179
Shale (Sh)	2.00×10^{-17}	0.103
Interbedded sandstone and shale (Ss/Sh)	7.00×10^{-15}	0.141

[a] Permeability is assumed to be isotropic.

The hydrogeological parameters (e.g., permeability and porosity) used in this study were estimated from the Taiwan Chelungpu fault Drilling Project (TCDP) Hole-A log samples, because the materials (e.g., sandstone and shale) are similar to those at the CCIP site. Due to the differences in geostress between the TCDP Hole-A and the CCIP site, the vertical geostatic pressure may affect the porosity and permeability of sedimentary rocks given different loading states and depths (Athy, 1930; Dickinson, 1953; Hoholick et al., 1984). Dong et al. (2010) performed a series of laboratory experiments and suggested that the power law function of geostress can be used to describe the permeability and porosity profiles as follows:

$$k = k_0 \left(\frac{Pe}{P_0} \right)^{-p} \tag{1}$$

and

$$\phi = \phi_0 \left(\frac{P_e}{P_0} \right)^{-q} \tag{2}$$

where P_0 is the atmospheric pressure [ML^{-1} T^{-2}]; P_e is the effective geostress [ML^{-1} T^{-2}] (P_e = 29.96 MPa as a constant value at the mean depth of the simulation formations), k is the permeability [L^2]; k_0 is the permeability under atmospheric pressure [L^2] ($k_0 = 3.04 \times 10^{-13}$ and 5.41×10^{-17} m^2 for sandstone and shale, respectively); ϕ is the porosity [−]; ϕ_0 is the porosity under atmospheric pressure [−] (ϕ_0 = 0.257 and 0.149 for sandstone and shale, respectively), p and q are the material parameters (p = 0.264, q = 0.064 for sandstone and p = 0.972, q = 0.065 for shale). Table 1 and Fig. 4 present the permeability and porosity estimated from the aforementioned conceptualized formations at the CCIP site. The porosity and permeability of the Sa–Sh are 0.141 (the average of sandstone and shale) and 7.0×10^{-15} m^2 (about one order less than for sandstone), respectively.

3.2. Numerical simulations with TOUGHREACT/ECO2N

The evolution of injected CO_2 in deep geological formations may involve displacement of saline brine (Bear, 1972; Juanes et al., 2006; Nordbotten and Celia, 2006; MacMinn et al., 2010; Zhang et al., 2011), buoyance/gravity convection (Riaz et al., 2006; Hesse et al., 2008; Elenius et al., 2010), and salt precipitation due to pore water dry-out (Pruess and Müller, 2009; Zhang et al., 2011). This possibility requires an appropriate numerical simulation to assess their impact. García and Pruess (2000) employed 2-D locally refined grids in geothermal reservoir simulations with the TOUGH2 code in their attempt to accurately represent the evolution of aquifer responses. In this study, 3-D locally refined grids are generated for sloping and layered heterogeneous formations in efforts to facilitate the efficacy of the TOUGHREACT/ECO2N simulator for field scale CGS simulations.

3.2.1. TOUGHREACT/ECO2N

TOUGHREACT is one of the TOUGH-family of codes developed by the Earth Sciences Division, Lawrence Berkeley National Laboratory (LBNL), in the USA. It inherits the multi-component, multi-phase fluid, and non-isothermal simulation capabilities of the TOUGH2 code and is equipped with a geochemical reactive-transport module. TOUGHREACT has been applied for the assessment of nuclear waste isolation, CGS, and groundwater contamination and remediation (Xu et al., 2006, 2011).

Equation-of-state (EOS) modules have been employed with the TOUGH-family of codes for particular hydrogeological environments or particular fluid-mixture problems in confined/unconfined aquifers or variably saturated geological media. ECO2N is one of the EOS modules of the TOUGH-family of codes (Pruess et al., 1999). It was designed for the simulation of CO_2 plume migration and the performance assessment of CO_2 sequestration in porous and fractured saline formations. The ECO2N module considers mixtures of H_2O–NaCl–CO_2 where the thermophysical properties are determined based on the state variables (e.g., pore pressure, temperature, salinity, and CO_2 gas saturation) of a system (Pruess, 2005). The limitations of the ECO2N module are that the pore pressure must be between 0.1 MPa and 60.0 MPa, and temperature must be between about 4 °C and 100 °C.

The governing equation for hydrodynamic transport in the TOUGH2 and TOUGHREACT simulators is based on mass conservation from the multiphase Darcy's law (Pruess et al., 1999; Xu et al., 2006, 2011). The continuum equations are discretized in space using the integral finite difference (IFD) method. The IFD method gives a flexible discretization for geological media that allows the use of either structured or unstructured volume grids (Narasimhan and Witherspoon, 1976). The time scale is discretized fully implicit as a first-order finite difference (Pruess et al., 1999).

The objective of this study is to serve as the preliminary phase of numerical investigations of CGS at the CCIP site. The purpose of this phase of numerical assessment is to obtain hydrogeological settings from seismic reflection surveys and then use them to investigate the migration of CO_2 plume affected by multiphase transport. At the current stage, the TOUGHREACT/ECO2N simulator is employed to perform simulations without the consideration of geochemical reactions. In the next phase of the project, the mineral components of the geological formation and chemical compositions of the formation water at the CCIP site will be utilized to identify the dominant geochemical reaction networks that must be considered. In order to use the same simulator for both the current and next phase of the project, the TOUGHREACT/ECO2N simulator is employed. Geochemical reactions are not considered in this study.

3.2.2. Simulation domain with locally refined grids

The TOUGH-family of codes allows users to discretize simulation domains with finite volume elements. Deformed elements were first proposed by McDonald and Harbaugh (1988) and Domenico and Schwartz (1988) as alternatives to orthogonal meshes or cuboids for the realistic simulation of aquifers or geological formations. In this study, locally refined grids are used to discretize the sloping and layered hydrogeological formations in the vicinity of the injection well with the geometric characteristics retrieved from seismic reflection surveys.

The geometry of the simulation domain is determined based on data from two seismic reflection survey lines (Fig. 3a and b). The simulation domain used in this study is 121 km^2 (i.e., 11 km × 11 km) as indicated by the black dashed lines (top-view) shown in Fig. 2. A side-view of the simulation domain in association with the survey lines and the location of the injection well are depicted in Fig. 3a; with dark blue solid lines and a black vertical line, respectively. The domain of interest is discretized with 3-level local refinement grids in the vicinity of the injection well that is located at the horizontal centroid of the domain, as shown in Fig. 5a, with half of the domain depicted in a perspective drawing. The x- and y-coordinates are set along the coastal shore and perpendicular to the coastal shore, respectively, as shown in Fig. 2. Fig. 5b shows the cross-sectional view of formations and grids at

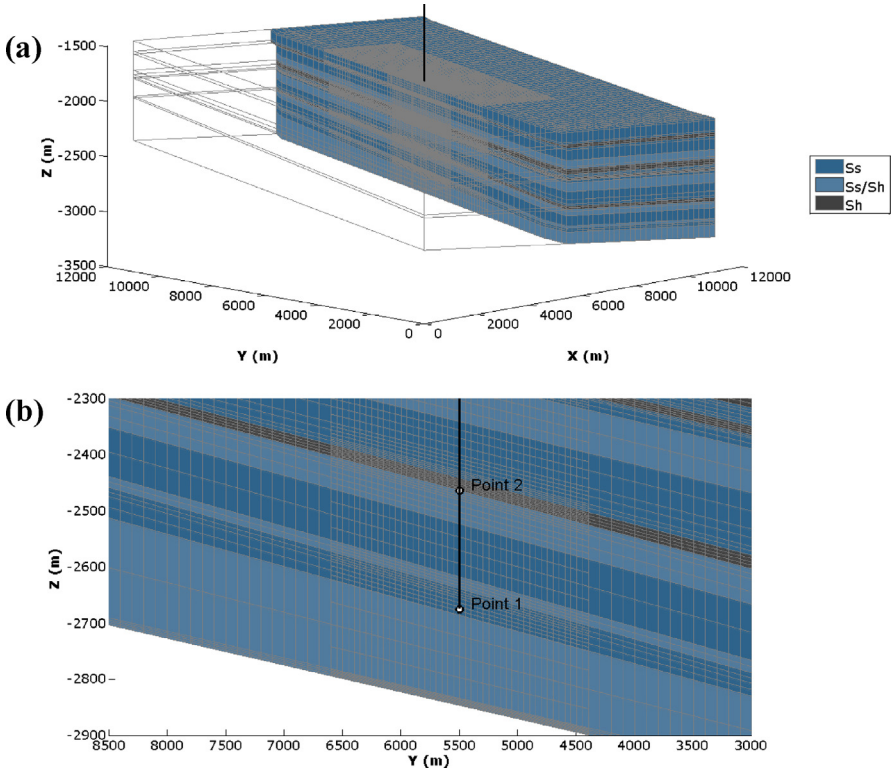

Fig. 5. Diagrams of the (a) simulation domain with locally refined grids and (b) cross sectional view of formations and grids at $x = 5500$ m (a) along line A–A′ (see Fig. 2). The black bold vertical line represents the CO_2 injection well.

$x = 5500$ m (Fig. 5a) along line A–A′ (see Fig. 2). Points 1 and 2 represent the location of the injection grid block and a grid block on the reservoir top right above the injection grid block, respectively, for later demonstration of simulated results.

According to seismic reflection surveys, the vertical depth of the simulation domain ranges from 3076 m at (11.0 km, 0.0 km) to 1364 m at (0.0 km, 11.0 km). The coarsest grids are defined as Level-0 grids composed of 57 rows, 57 columns, and 32 vertical layers with different porosities and permeabilities, as shown in Fig. 5. The bottom depth of each formation and the thickness of each divided layer are estimated with bilinear interpolation of formations identified from both survey lines (i.e., OR1-928-16 and OR1-928-1, shown in Figs. 2 and 3). The Level-1 grids cover the horizontal domain of (2 km, 3 km) and (8 km, 9 km) and the entire vertical domain. Each Level-0 grid is divided into 8 Level-1 grids. The Level-2 grids cover the horizontal domain of (4.4 km, 4.4 km) and (6.6 km, 6.6 km) and the entire vertical domain by dividing each Level-1 grid into 8 Level-2 grids. Table 2 lists the spatial resolution of the 3-level local refinement grids with a total of 522,400 grids used in this study.

3.3. Model parameters and simulation setup

As mentioned in the CCIP site description, the target CO_2 reservoir contains formations beneath the Chinshui Fm. (functioning as the low permeability caprock) and above the bedrock. Taking the rock properties profiles shown in Fig. 4 as an example, the potential CO_2 reservoir is from 2490 m to 2840 m below the mean sea level at the location of the injection well. The porosity and permeability of each type of rock are listed in Table 1 and isotropic characteristic is assumed. Both Level-1 and Level-2 grids inherit the same material properties assigned to Level-0 grids. The simulation is performed for a time period of 500 years. A single CO_2 injection well with a constant rate of 1 Mt/yr is assumed for the first 50 years. CO_2 injection is applied into a single grid block at a depth of 2674 m below the mean sea level, shown as point 1 in Fig. 5b. At the current stage of simulations, isothermal conditions with an ambient temperature of 70 °C and a salinity of 3.0% are used throughout the domain of interest. Stagnant groundwater flow conditions are assumed due to the reservoir being located in a deep saline brine aquifer. Initial pore pressure distributions are obtained by performing a steady state simulation without injection and with no flow boundary conditions. Fig. 6 shows the initial pore pressure distributions parallel to rock formations, ranging from 18.8 MPa to 28.7 MPa corresponding to the depths of 1717 m and 3241 m, respectively, below the mean sea level. Subsequent simulations are then performed with the prescribed Dirichlet conditions from the prior simulation on the lateral sides and with impermeable boundary conditions on both the top and bottom sides. The van Genuchten-Mualem model (Mualem, 1976; van Genuchten, 1980) and the van Genuchten function (van Genuchten, 1980) are employed to describe changes of relative permeability and capillary pressure, respectively, that occur due to variations of saturation in the multiphase saline brine-CO_2 system.

Table 2
Spatial resolution for the 3-level refined grids.

	Level-0	Level-1	Level-2
Horizontal resolution	200 m × 200 m	100 m × 100 m	50 m × 50 m
Vertical refinement	32 layers	1/2 of Level-0	1/2 of Level 1
Equivalent sub-grid numbers	8 Level-1 grids	8 Level-2 grids	1
Coordinates of horizontal corner nodes	(0.0 km, 0.0 km); (11.0 km, 11.0 km)	(2.0 km, 3.0 km); (8.0 km, 9.0 km)	(4.4 km, 4.4 km); (6.6 km, 6.6 km)

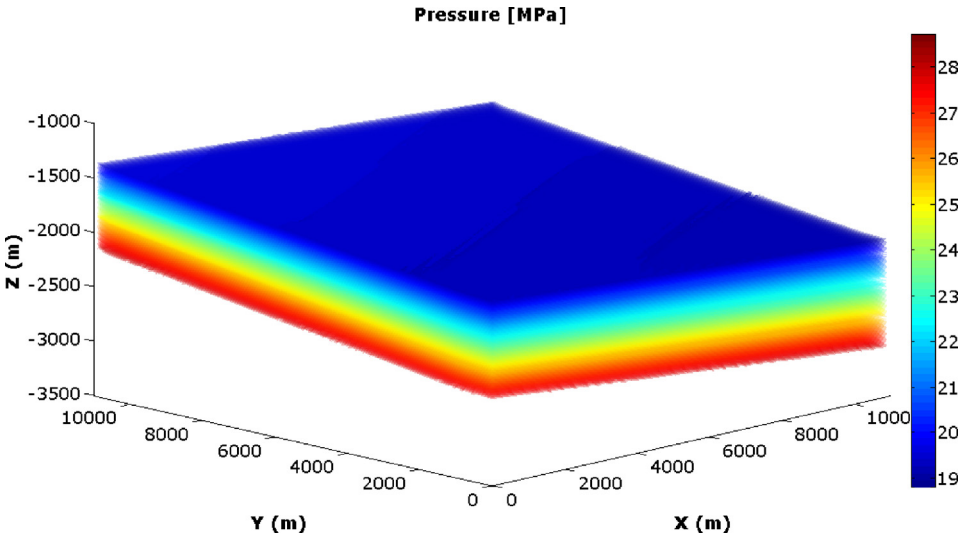

Fig. 6. Initial pore pressure distribution.

The parameters used for the TOUGHREACT/ECO2N simulator are listed in Table 3.

Injection of CO_2 into saline brine aquifers may cause pore water dry-out and salt precipitation, which may reduce formation porosity and permeability (Verma and Pruess, 1988; Pruess and Müller, 2009). In this study, we employ the Brooks–Corey-like relationship (Brooks and Corey, 1966) (also known as the power law) to describe the change of permeability, k, that occurs due to salt dissolution/precipitation as calculated with the following equation (Pruess, 2005):

$$k = k_i(1 - S_s)^{\gamma} \tag{3}$$

where k_i is the initial permeability [L^2]; S_s is the solid saturation [−]; γ is the regression parameter ($\gamma = 0.8$ in this study).

3.4. Assessment of CO_2 trapping

The feasibility of CGS in deep saline brine aquifer relies on successful retention of injected CO_2 in geological formations which may involve different trapping mechanisms, namely hydrodynamic, residual gas, solubility, and mineral trappings (Holloway and Savage, 1993; Bachu et al., 1994; Class et al., 2009; Yamamoto et al., 2009; Xu et al., 2011). At the current stage of simulation, when geochemical reactions are not considered, the amount of mineral trapping is neglected. Grid-based estimations of total CO_2 trapping amount contributed by different trapping mechanisms are given as below.

Hydrodynamic trapping, H_{CO_2} [M], accounts for the injected CO_2 trapped as a mobile gas or supercritical fluid by the low permeability caprock, and is estimated using the following equation:

$$H_{CO_2} = \sum_n (S_{g,n} - S_{gr,n}) V_n \phi_n \rho_{g,n} \quad \text{when } S_{g,n} > S_{gr,n} \tag{4}$$

Residual gas trapping, R_{CO_2} [M], accounts for the immobile state of CO_2 as part of the injected CO_2 becoming disconnected or having residual droplets in the pore spaces, and is parameterized by the irreducible gas saturation as shown in the following equation:

$$R_{CO_2} = \sum_n \min(S_{g,n}, S_{gr,n}) V_n \phi_n \rho_{g,n} \tag{5}$$

Solubility trapping, D_{CO_2} [M], accounts for the effective dissolution of injected CO_2 in formation water after deducting the initial dissolved CO_2 mass in the domain as in the following equation:

$$D_{CO_2} = \left(\sum_n S_{l,n} V_n \phi_n \rho_{l,n} X_{CO_2,n} \right) - D_{CO_2,\text{init}} \tag{6}$$

where S_g, S_{gr}, and S_l are the gas saturation [−], irreducible gas saturation [−], and liquid saturation [−], respectively; V is the mesh volume [L^3]; ϕ is the porosity [−]; ρ_g and ρ_l are the gas density and liquid density [ML^{-3}], respectively; X_{CO_2} is the dissolved CO_2 mass fraction [−]; and $D_{CO_2,\text{init}}$ is the initial dissolved CO_2 mass in the domain [M]. The subscript n represents the grid index.

Table 3
Parameters used for the TOUGHREACT/ECO2N simulator.

Parameters	Values
Number of grid	522,400
Number of connection	1,552,346
Grid resolution (horizontal)	See Table 2
Depth of injection well	−2674 m (m.s.l.)
Pressure distribution	18.8 MPa (−1717 m) ~28.7 MPa (−3241 m)
Temperature distribution	Isothermal (70 °C)
Salinity	30‰
Initial CO_2 mass fraction in the brine	0.0454%
Injection rate	1 Mt/yr (~31.71 kg/s)
Injection period	Fist 50 year
Simulation period	500 year
Relative-permeability vs. saturation curve: van Genuchten-Mualem model (van Genuchten, 1980; Corey, 1954)	
Irreducible water saturation	0.200
Exponent coefficient	0.400
Irreducible gas saturation	0.050
Capillary vs. saturation curve: van Genuchten function (van Genuchten, 1980)	
Air-entry potential	19.59 kPa for sandstone, 61.95 kPa for Sa–Sh, 1959.00 kPa for shale

Note that "Sa–Sh" denotes the interbedded sandstone and shale.

4. Results and discussion

The numerical simulation carried out to investigate the evolution of injected CO_2 at CCIP site with its sloping and layered heterogeneous formation cover a time period of 500 years, with CO_2 injection for the first 50 years. The simulation results are discussed focusing on the following important points: (1) the aquifer responses due to CO_2 injection; (2) the post injection migration of

CO_2 plume; and (3) the evolution of different CO_2 trapping mechanisms.

4.1. Injection period

During the early stages of injection, the pore pressure built up rapidly due to the increase of viscous forces and the capillary pressures of the two slightly miscible fluids of saline brine and supercritical CO_2 caused by the CO_2 injection (Bear, 1972; Juanes et al., 2006; Nordbotten and Celia, 2006; Zhang et al., 2011; Kolditz et al., 2012). Fig. 7 presents the time evolution of aquifer responses, including pore pressure, CO_2-rich gas saturation, dissolved CO_2 mass fraction, and solid saturation, at the injection grid block (Point 1 in Fig. 5b) and at a grid block of the reservoir top right above the injection grid block (Point 2 in Fig. 5b). Injected supercritical CO_2 causes the pore pressure to increase and the dissolved CO_2 mass fraction at the injection grid block as shown in Fig. 7a and b, respectively. The subsequent decrease of liquid saturation at the injection grid block (Fig. 7b) explains the displacement of formation water and the rising of CO_2-rich gas saturation (Fig. 7c). The maximum pore pressure appears at 32.4 days with an increase of 3.33 MPa with respect to the initial pore pressure at the injection grid block. The pore pressure then gradually declines with migration of CO_2 to layers below and above the injection grid block due to gravitational and buoyancy forces. Salt precipitation, with the evolution of the solid saturation and NaCl mass fraction, shown in Fig. 7d, appears at 2.1 years as a consequence of the drying out of pore water (Fig. 7b) in association with the continuing increase of gas saturation (Fig. 7c) at the injection grid block. At the end of the injection process, 0.023 of pore volume is occupied by solid saturation at the injection grid block.

The evolution over time of the increase of pore pressure at the reservoir top is relatively small and lags behind that at the injection grid block, as can be seen in Fig. 7a. The difference in maximum pore pressure at the reservoir top is 1.36 MPa. The migration of upwelling CO_2 reaches the reservoir top at 4.6 years, causing an abrupt increase in the dissolved CO_2 mass fraction, as shown in Fig. 7b. The subsequent increase in the CO_2-rich gas saturation reaches its maximum value of around 0.6 at 50 years (Fig. 7c). Salt precipitation does not appear at the reservoir top, as shown in Fig. 7d.

Fig. 8a presents a cross-sectional view (at $x = 5500$ m) of the increase in pore pressure at 50 years. The slightly bottlenecked distribution of pore pressure differences is caused by the presence of a thin Ss/Sh layer, which has a low permeability and porosity than that of the rest of the reservoir with its Ss formations (Fig. 4 and Table 1). Taking pore pressure changes of grids along the injection well at the end of the injection for examples, a pore pressure change of about 1.3 MPa is observed at the reservoir top and part of bottom grids of the low permeability caprock, while an increase of 0.07 MPa is observed at the bottom of the Ss layer right above the low permeability caprock, as shown in Fig. 8a. The injection-induced pore pressure changes are successfully retained along the sloping low permeability caprock. Fig. 8b and c present the distribution of CO_2-rich gas saturation and dissolved CO_2 mass fraction, respectively, at 50 years. In the vicinity of the injection grid block, the high gas saturation and a low dissolved mass fraction are simultaneously observed, which can be explained by the full displacement of formation water by supercritical CO_2. The distribution of gas saturation is mostly affected by the sloping and layered heterogeneous formations, as shown in Fig. 8b. Although isotropic permeability is assumed, the presence of layered heterogeneous formations is propitious for the migration of supercritical CO_2 along sloping formations and then entering different layers with lower permeability. Unlike the layered distribution of gas saturation, the dissolved CO_2 mass fraction presents a relatively uniform

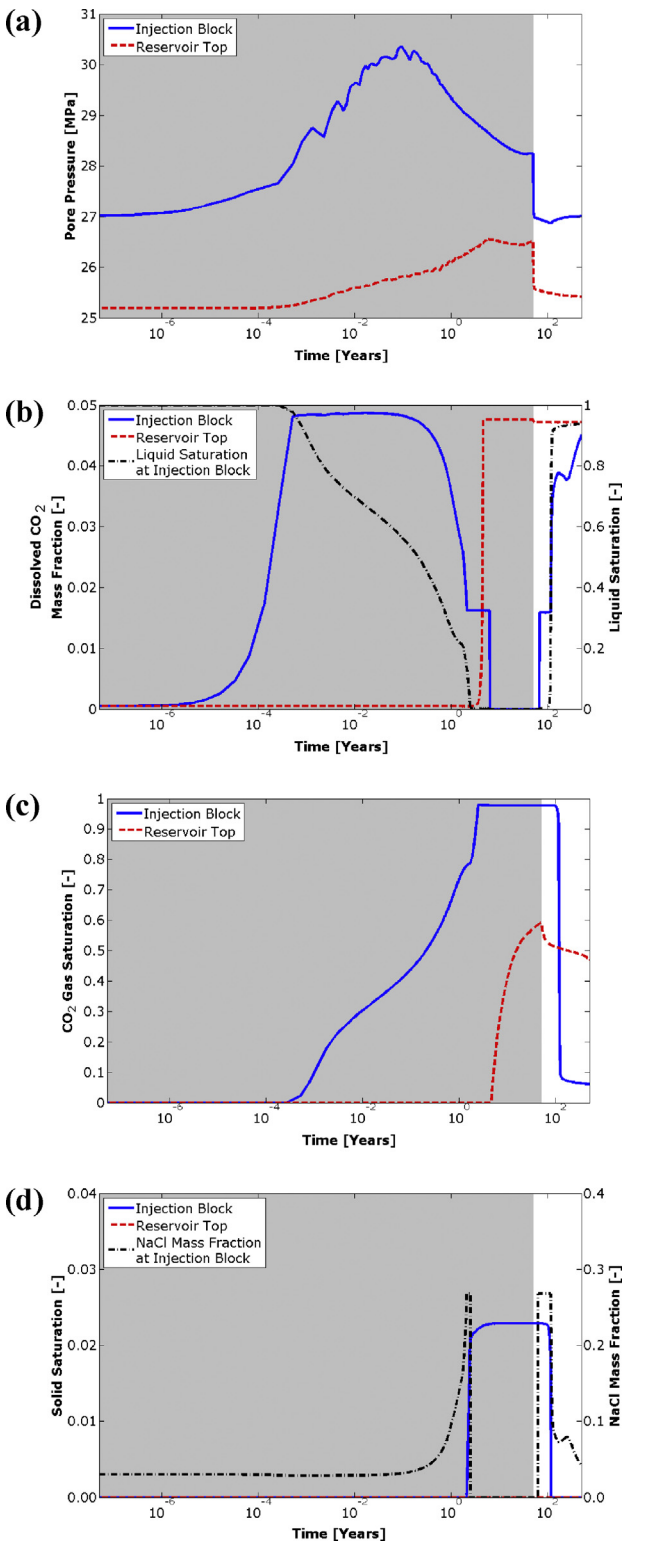

Fig. 7. Time evolution of aquifer responses at injection block (Point 1 in Fig. 5b) and reservoir top (Point 2 in Fig. 5b), including: (a) pore pressure, (b) dissolved CO_2 mass fraction and liquid saturation, (c) CO_2-rich gas saturation, and (d) solid saturation and NaCl mass fraction. The shaded area indicates the CO_2 injection period of 50 years.

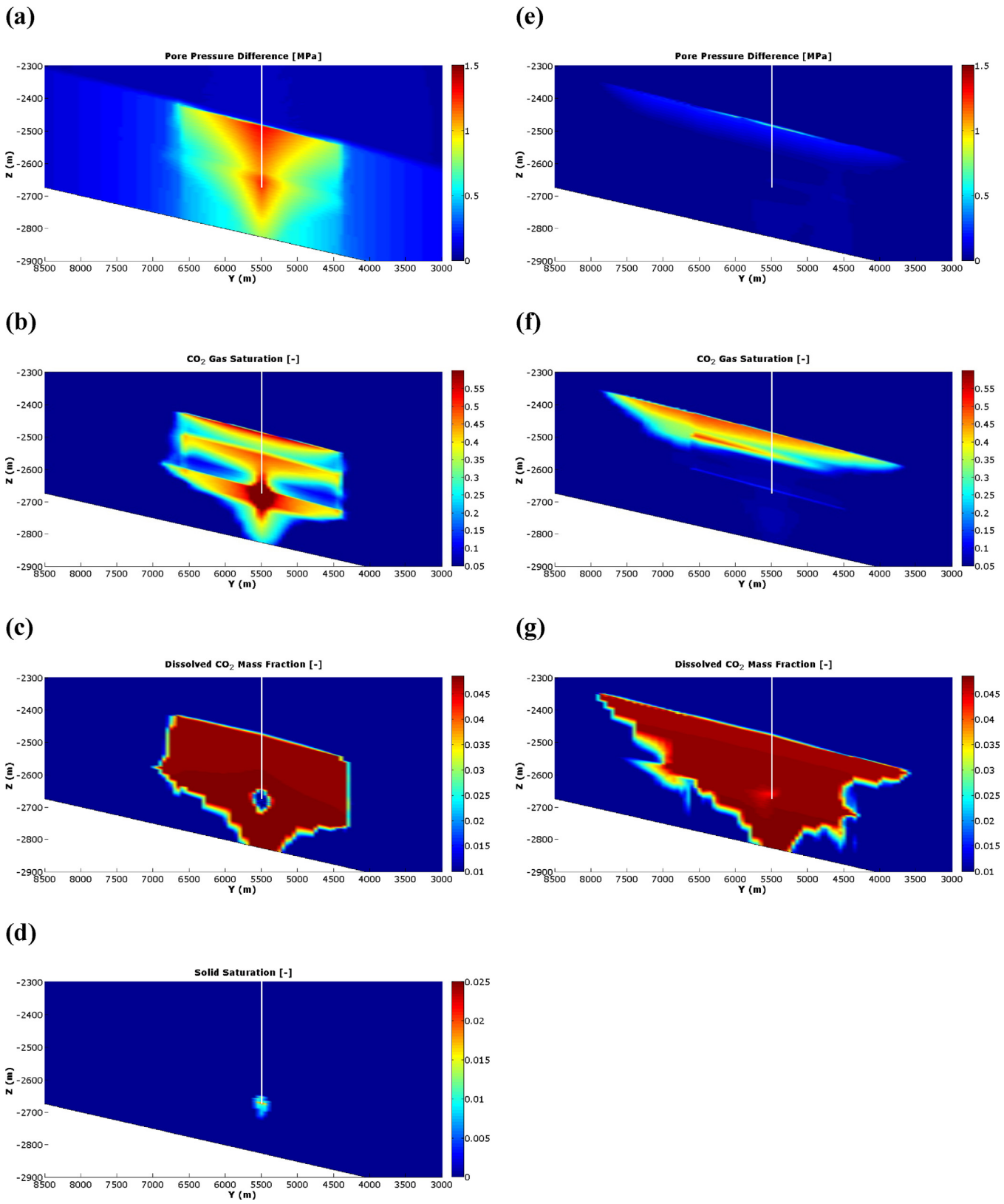

Fig. 8. Cross-sectional view of profiles at $x = 5500$ m showing spatial distribution of aquifer responses at 50 years ((a)–(d)) and 500 years ((e)–(g)): (a) and (e) are pore pressure difference, (b) and (f) are CO_2-rich gas saturation, (c) and (g) are dissolved CO_2 mass fraction, and (d) is solid saturation. The vertical white line indicates the location of the injection well.

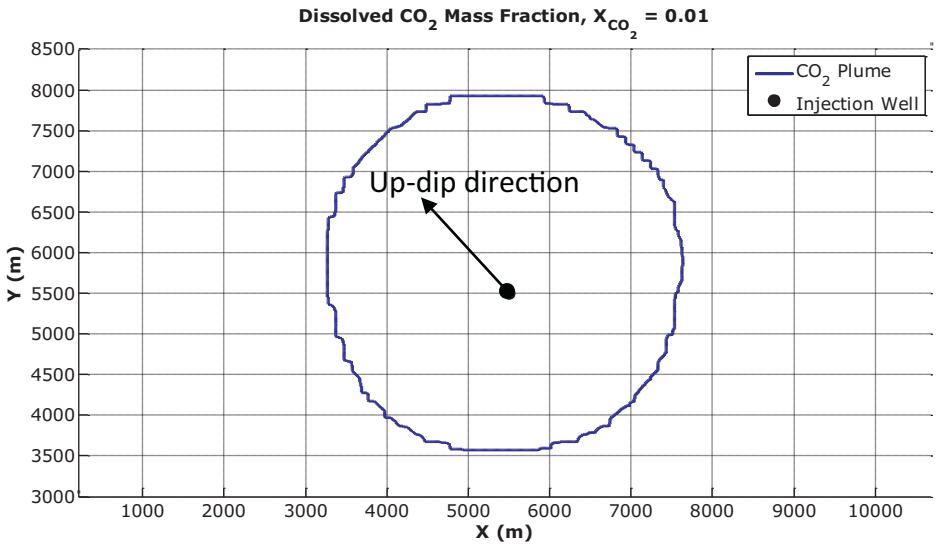

Fig. 9. Bird's eye views of the spread of the CO_2 plume (dissolved CO_2 mass fraction of 0.01) beneath the low permeability caprock at 500 years.

distribution with a sharp front at the plume boundary, as shown in Fig. 8c. Salt precipitation is observed in the vicinity of the injection grid block as a consequence of the drying out of pore water (see Fig. 8d).

4.2. Post injection migration

The dominant flow mechanisms affecting the post injection migration of CO_2 plume are viscous flow of fluid and buoyant flows of CO_2 as the injection pressure dissipates (Hesse et al., 2008; MacMinn et al., 2010, 2011; Pruess and Nordbotten, 2011; Xu et al., 2011). After injection ceases, the pore pressure drops quickly at both the injection block and the reservoir top, as shown in Fig. 7a. Backflow during the aqueous phase causes the dissolution of precipitated salt (Fig. 7d), the increase of dissolved CO_2 mass fraction (Fig. 7b), and the reduction of gas saturation to the prescribed irreducible gas saturation (Fig. 7c) at the injection block. The rise of liquid saturation at the injection block (Fig. 7b) explains the appearance of aqueous backflow after injection ceases. At the grid block of the reservoir top, dissolved CO_2 mass fraction remains high (Fig. 7b) and gas saturation gradually decrease with time (Fig. 7c).

Fig. 8e presents a cross-sectional view (at $x = 5500$ m) of the remaining pore pressure differences at 500 years, showing substantial dissipation of injection pressure throughout the domain. The distribution of CO_2-rich gas saturation shows the accumulation of supercritical CO_2, mainly retained beneath the low permeability caprock, which has migrated further toward the up-dip direction, as depicted in Fig. 8f. Dissolved CO_2 will raise the density of saline brine higher than that of ambient formation water. Sustained CO_2 dissolution may induce vertical dripping from the bottom faces of CO_2 plume because of the effect that dissolved CO_2 has on brine density (Riaz et al., 2006; Elenius et al., 2010; Pruess and Nordbotten, 2011). Significant vertical dripping is observed at both the downslope and upslope sides of the injection well (see Fig. 8g), for the distribution of the dissolved CO_2 mass fraction at 500 years.

The maximum migration distance and the extent of the CO_2 plume could be affected by the sloping formations (Doughty et al., 2004; MacMinn et al., 2010, 2011; Pruess and Nordbotten, 2011). Simulation results show the maximum migration distance of the CO_2 plume is about 2550 m away from the injection grid block toward the up-tilt direction (roughly the West in Fig. 2) of the sloping formations as depicted in Fig. 9. The extent of the CO_2 plume on the top layer of the reservoir presents an irregular circle that is roughly symmetrical with respect to the formation dip direction (East–West) as depicted in Fig. 9, and shows the contour of dissolved CO_2 with a mass fraction of 0.01 at 500 years.

4.3. Time evolution of CO_2 trapping mechanisms

The evaluation of injected CO_2 retained by different trapping mechanism is important to confirming the feasibility of CGS in deep saline brine aquifers, which may involve a mixture of hydrodynamic, residual gas, solubility, and mineral trapping. The amount of mineral trapping which might actually occur is neglected at the current stage in the simulation process meaning that geochemical reactions are not considered. The mass of trapped components contributed by hydrodynamic, residual gas, and solubility are estimated by summing each component throughout the domain grids as described in Eqs. (4)–(6), respectively. A total of 50 million tons of CO_2 is injected for a time period of 50 years. Comparison of the time evolution of different trapping mechanisms from 50 years to 500 years is depicted in Fig. 10. Hydrodynamic trapping accounts for 69.5% of injected CO_2 by weight at 50 years and is reduced to 54.2% at 500 years. On the other hand, contributions of

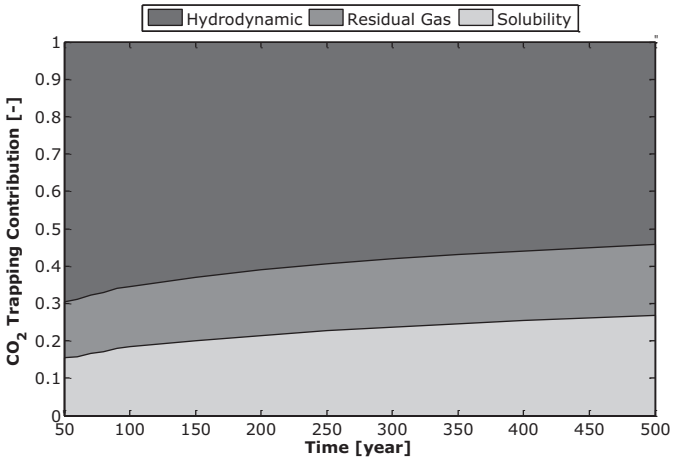

Fig. 10. Comparison of CO_2 trapping contributed by different trapping mechanisms.

solubility trapping and residual gas trapping increase from 15.6% to 26.8% and from 14.9% to 19%, respectively, due to migration of CO_2 plume. The reduction of hydrodynamic trapping is mainly transformed into solubility trapping with expansion in extent of the dissolved CO_2 mass fraction, as shown in Fig. 8c and g.

5. Conclusions

The conclusions from this preliminary numerical assessment of CGS in Taiwan are summarized below.

(1) Field scale CGS simulations of the CCIP site are facilitated with locally refined grids in the vicinity of the CO_2 injection well to successfully capture the time evolution of aquifer responses and plume migration. This method has the advantage of computational efficiency. The fate of injected CO_2 in deep saline brine aquifers is significantly affected by the sloping and layered heterogeneous formations at the CCIP site, as shown in the simulation results in Fig. 8.
(2) The CO_2 plume is successfully retained by the low permeability caprock (Chinshui Shale), migrating laterally along the bottom face of the sloping caprock to create an approximately round and asymmetric pattern in the top-view.
(3) Significant vertical dripping is observed on both the downslope and upslope sides of the injection well due to the effects of dissolved CO_2 on rising brine density.
(4) Salt precipitation appears in the vicinity of the injection grid block as a consequence of the drying out of pore water, causing a reduction of formation porosity and permeability that enhance the build-up of pore pressure during CO_2 injection.
(5) After injection ceases, the reduction of hydrodynamic trapping is mainly compensated for by the increase in solubility trapping. Solubility and residual gas trapping account for a total of 46% of injected CO_2 by weight at 500 years, increasing from a total of 30.5% at 50 years.
(6) At the current stage of simulations, isothermal conditions with an ambient temperature of 70 °C are assumed throughout the domain of interest, and the effects of geothermal gradients are not considered. In the next phase of the simulation, data on the in situ geothermal gradient, the mineral components of the geological formations, and the chemical compositions of the formation water at the CCIP site will be available for pursuing coupled thermal, hydrological, and geochemical simulations.
(7) The potential offshore fault identified by the B–B′ seismic reflection survey is not considered in the current stage because the fault is far away from the CCIP site. However future investigations to assess the risk of CO_2 leakage should consider larger simulation domains and longer simulation times.

Acknowledgements

This work was funded by the National Science Councilunder grant NSC-101-3113-E-008-002 through National Central University. The authors are grateful to the editor and two anonymous reviewers for their comments and suggestions.

References

Athy, L.F., 1930. Density, porosity, and compaction of sedimentary rocks. AAPG Bulletin 14, 1–24.
Bachu, S., Gunter, W.D., Perkins, E.H., 1994. Aquifer disposal of CO_2: hydrodynamic and mineral trapping. Energy Conversion and Management 35 (4), 269–279.
Bear, J., 1972. Dynamics of Fluids in Porous Media. Elsevier, New York, 784 pp. (reprinted with corrections, Dover, New York, 1988).
Bonilla, M.G., 1975. A Review of Recently Active Fault in Taiwan. Open-File Report 75-41. U. S. Geological Survey, Menlo Park, CA.
Brooks, R.H., Corey, A.T., 1966. Properties of porous media affecting fluid flow. Journal of Irrigation and Drainage Engineering (ASCE) 92, 61–88.
Celia, M.A., Nordbotten, J.M., 2009. Practical modeling approaches for geological storage of carbon dioxide. Ground Water 47 (5), 627–638.
Cheng, C.-T., Chiou, S.-J., Lee, C.-T., Tsai, Y.-B., 2007. Study on probabilistic seismic hazard maps of Taiwan after Chi–Chi earthquake. Journal of GeoEngineering 2 (1), 19–28.
Chiao, C.-H., Lin, J.-Y., Yu, C.-W., Lu, C.-Y., 2010. Carbon dioxide sequestration assessment of late miocene to pleistocene sedimentary strata in the southern flank of the Tai-Hsi Basin. Mining & Metallurgy 55 (1), 109–128 (in Chinese).
Class, H., Ebigbo, A., Helmig, R., Dahle, H.K., Nordbotten, J.M., Celia, M.A., Audigane, P., Darcis, M., Ennis-King, J., Fan, Y., Flemisch, B., Gasda, S.E., Jin, M., Krug, S., Labregere, D., Beni, A.N., Pawar, R.J., Sbai, A., Thomas, S.G., Trenty, L., Wei, L., 2009. A benchmark study on problems related to CO_2 storage in geologic formations. Computers & Geosciences 13, 409–434.
Corey, A.T., 1954. The interrelation between gas and oil relative permeabilities. Producers Monthly 19 (1), 38–41.
Dickinson, G., 1953. Geological aspects of abnormal reservoir pressures in Gulf Coast Louisana. AAPG Bulletin 37 (2), 410–432.
Domenico, P.A., Schwartz, F.W., 1988. Physical and Chemical Hydrogeolooy, 2nd ed. John Wiley & Sons, New York, 528 pp.
Dong, J.-J., Hus, J.-Y., Wu, W.-J., Shimamoto, T., Hung, J.-H., Yeh, E.-C., Wu, Y.-H., Sone, H., 2010. Stress-dependence of the permeability and porosity of sandstone and shale from TCDP Hole-A. International Journal of Rock Mechanics & Mining Sciences 47, 1141–1157.
Doughty, C., Pruess, K., Benson, S.M., Freifeld, B.M., 2004. Hydrological and geochemical Monitoring for a CO_2 Sequestration Pilot in a Brine Formation. Technical Report LBNL-55104. Lawrence Berkeley National Laboratory, Berkeley, CA.
Elenius, M.T., Tchelepi, H.A., Johannsen, K., 2010. CO_2 trapping in sloping aquifers: high resolution numerical simulations. In: XVIII International Conference on Water Resources, CMWR 2010.
García, J., Pruess, K., 2000. Local Grid Refinement for Multi-Scale Geothermal Reservoir Simulation with TOUGH2. Technical Report LBNL-45646. Lawrence Berkeley National Laboratory, Berkeley, CA.
Gasda, S.E., Nordbotten, J.M., Celia, M.A., 2011. Vertically averaged approaches for CO_2 migration with solubility trapping. Water Resources Research 47, W05528.
Hesse, M.A., Orr jr., F.M.F.M., Tchelepi, H.A., 2008. Gravity currents with residual trapping. Journal of Fluid Mechanics 611, 35–60.
Hoholick, J.D., Metarko, T., Potter, P.E., 1984. Regional variations of porosity and cement: St. Peter and Mount Simon sandstones in Illinois Basin. AAPG Bulletin 68 (6), 753–764.
Holloway, S., Savage, D., 1993. The potential for aquifer disposal of carbon dioxide in the UK. In: Riemer, W.F. (Ed.), Proceedings of the International Energy Agency Carbon Dioxide Disposal Symposium, Pergamon Press, Oxford. Energy Conservation and Management 34 (9–11), 925–932.
Juanes, R., Spiteri, E.J., Orr Jr., F.M., Blunt, M.J., 2006. Impact of relative permeability hysteresis on geological CO_2 storage. Water Resources Research 42, W12418.
Kolditz, O., Görke, U.-J., Shao, H., 2012. Thermo-Hydro-Mechanical–Chemical Processes in Porous Media: Benchmarks and Examples. Springer, Heidelberg, Germany, 404 pp.
Lin, A.T., Watts, A.B., 2002. Origin of the West Taiwan Basin by orogenic loading and flexure of a rifted continental margin. Journal of Geophysical Research 107 (B9), ETG 2-1–ETG 2-19.
Lin, A.T., Watts, A.B., Hesselbo, S.P., 2003. Cenozoic stratigraphy and subsidence history of the South China Sea Margin in the Taiwan region. Basin Research 15, 453–478.
Lin, C.-W., Chang, H.-C., Lu, S.-T., Shih, T.-S., Shih, W.-J., 2000. Active Fault Map of Taiwan, 2nd ed. Central Geological Survey Special Publication, No. 13, 122 pp.
MacMinn, C.W., Szulczewski, M.L., Juanes, R., 2010. CO_2 migration in saline aquifers. Part 1. Capillary trapping under slope and groundwater flow. Journal of Fluid Mechanics 662, 329–351.
MacMinn, C.W., Szulczewski, M.L., Juanes, R., 2011. CO_2 migration in saline aquifers. Part 2. Capillary and solubility trapping. Journal of Fluid Mechanics 688, 321–351.
McDonald, M.G., Harbaugh, A.W., 1988. A Modular Three-Dimensional Finite Difference Ground-Water Flow Model. Techniques of Water-Resources Investigations 06-A1. U. S. Geological Survey, 576 pp.
Mualem, Y.A., 1976. A new model for predicting hydraulic conductivity of unsaturated porous media. Water Resources Research 12 (3), 513–522.
Narasimhan, N.T., Witherspoon, P.A., 1976. An integrated finite difference method for analyzing fluid flow in porous media. Water Resources Research 12 (1), 57–64.
Nicot, J.P., 2008. Evaluation of large-scale CO_2 storage on fresh-water sections of aquifers: an example from the Texas Gulf Coast Basin. International Journal of Greenhouse Gas Control 2 (4), 582–593.
Nordbotten, J.M., Celia, M.A., 2006. Similarity solutions for fluid injection into confined aquifers. Journal of Fluid Mechanics 561, 307–327.
Pruess, K., 2005. ECO2N: A TOUGH2 Fluid Properties Module for Mixtures of Water, NaCl, and CO2. Report LBNL-57592. Lawrence Berkeley National Laboratory, Berkeley, CA.
Pruess, K., García, J., 2002. Multiphase flow dynamics during CO_2 disposal into saline aquifers. Environmental Geology 42, 282–295.
Pruess, K., Müller, N., 2009. Formation dry-out from CO_2 injection into saline aquifers: 1. Effects of solids precipitation and their mitigation. Water Resources Research 45, W03402.

Pruess, K., Nordbotten, J., 2011. Numerical simulation studies of the long-term evolution of a CO_2 plume under a sloping caprock. Transport in Porous Media 90, 135–151.

Pruess, K., Oldenburge, C., Moridis, G., 1999. TOUGH2 User's Guide Version 2.0. Report LBNL-43134. Lawrence Berkeley National Laboratory, Berkeley, CA.

Riaz, A., Hesse, M., Tchelepi, H.A., Orr jr., F.M., 2006. Onset of convection in a gravitationally unstable diffusive boundary layer in porous media. Journal of Fluid Mechanics 548, 87–111.

Taiwan Power Company, 2008. Taiwan Power Company Sustainability Report 2007.

Taiwan Power Company, 2009. Taiwan Power Company Sustainability Report 2008.

Taiwan Power Company, 2010. Taiwan Power Company Sustainability Report 2009.

Taiwan Power Company, 2011. Taiwan Power Company Sustainability Report 2010.

Taiwan Power Company, 2012. Taiwan Power Company Sustainability Report 2011.

Taiwan Power Company, 2013. Taiwan Power Company Sustainability Report 2012.

Todaka, N., Nakanishi, S., Xu, T., Pruess, K., 2009. Hydrogeochemical modeling for natural analogue study of CO_2 leakage due to Matsushiro earthquake swarm. Greenhouse Gas Control Technologies 9. Energy Procedia 1, 2413–2420.

van Genuchten, M.T.H., 1980. A closed-form equation for predicting the hydraulic conductivity of unsaturated soils. Soil Science Society of America Journal 44, 892–898.

Verma, A., Pruess, K., 1988. Thermohydrologic conditions and silica redistribution near high-level nuclear wastes emplaced in saturated geological formations. Journal of Geophysics Research 93 (B2), 1159–1173.

Wang, C.-Y., Shin, T.-C., 1998. Illustrating 100 years of Taiwan seismicity. Journal of Terrestrial, Atmospheric and Oceanic Sciences 9, 589–614.

Xu, T., Sonnenthal, E., Spycher, N., Pruess, K., 2006. TOGUREACT User's Guide: A Simulation Program for Non-isothermal Multiphase Reactive Geochemical Transport in Variably Saturated Geologic Media. Report LBNL-55460. Lawrence Berkeley National Laboratory, Berkeley, CA.

Xu, T., Spycher, N., Sonnenthal, E., Zhang, G., Zheng, L., Pruess, K., 2011. TOUGHREACT version 2.0: a simulator for subsurface reactive transport under non-isothermal multiphase flow conditions. Computers & Geosciences 37, 763–774.

Yamamoto, H., Zhang, K., Karasaki, K., Marui, A., Uehara, H., Nishikawa, N., 2009. Numerical investigation concerning the impact of CO_2 geologic storage on regional groundwater flow. International Journal of Greenhouse Gas Control 3, 586–599.

Yu, C.-W., Chen, S., Shao, K.-S., Chiao, C.-H., Hwang, L.-T., Chen, J.-L., 2011. Development of CCS technology for coal-fired power plant in Taiwan. Energy Procedia 4, 4806–4813.

Zhang, K., Moridis, G., Pruess, K., 2011. TOUGH + CO_2: a multiphase fluid-flow simulator for CO_2 geologic sequestration in saline aquifers. Computers & Geosciences 37, 714–723.